Supporting Information

Efficient Fe-N_4 Site Activated by Te Doping with Polarity Engineering for Enhanced Nitrate Electroreduction Reaction

Ziyi Wang,[1] Zhenhai Fan,[1] Xiaomeng Guo,[2]* Shengjie Wei,[3] Junxiong Ke,[4,5] Jijie Zhang[1]*

Address

1. *School of Materials Science and Engineering, Nankai University, Tianjin 300350, P. R. China*

2. *College of Chemistry and Pharmaceutical Engineering, Hebei University of Science and Technology, Shijiazhuang 050018, China*

3. *Center Excellence for Environmental Safety and Biological Effects, Beijing Key Laboratory for Green Catalysis and Separation, Department of Chemistry, College of Chemistry and Life Science, Beijing University of Technology, Beijing 100124, P. R. China*

4. *Shandong Tsaker New Materials Co., Ltd., Dongying, Shandong province 257200, China*

5. *School of Chemical Engineering and Technology, State Key Laboratory of Chemical Engineering, Tianjin University, Tianjin 300072, China.*

EXPERIMENTAL SECTION

Method

Reagents. $Zn(NO_3)_2 \cdot 6H_2O$ (Aladdin, 99.99%), 2-methylimidazole (Acros, 99%), Te (Heowns, 99.9%), iron(III) acetylacetonate ($Fe(acac)_3$, Acros, 99+%), methanol (Beijing Chemical Reagent, AR), ethanol (Beijing Chemical Reagent, AR), N,N-dimethylformamide (DMF, Sinopharm Chemical, AR), argon gas (99.999%), Nafion D-521 dispersion (5% w/w in water and 1-propanol, Alfa Aesar), potassium nitrate (Aladdin, 99+%), sodium sulfate anhydrous (Aladdin, 99%), ammonium sulfate (Macklin, 99.99+%), Sulfuric acid (Chemical Reageng, AR), sodium hydroxide (Aladdin, 96%), salicylic acid (Macklin, AR), sodium citrate teibasic dihydrate (Macklin, 99+%), sodium hypochlorite (Macklin, 30+%), sodium nitroferricyanide (III) dihydrate (Macklin, AR), N-(1-Naphthyl) ethylenediamine dihydrochloride (TCL, 98.0+%), phosphoric acid (Aladdin, 85+wt.% in H_2O), sulfanilamide (Vetec, 97%). The drugs were used directly without further purification. The deionized water used for NRA had a resistivity of 18.2 MΩ cm^{-1}, achieved through ion-exchange and filtration processes.

Preparation of Te@ZIF-8

In beaker A, $Zn(NO)_3 \cdot 6H_2O$ (5.58 g) and Te (2.00 g) were dissolved in 150 mL of the methyl alcohol. In beaker B, 2-methylimidazole was dissolved in 150 mL of the methyl alcohol. After ultrasonically dissolving the solutions in the two beakers respectively, pour the solution in beaker B into beaker A and stir at room temperature for 24 h. The stirred solution was centrifuged, washed five times with ethanol, and dried in an oven

at 50 ℃ for 12 h to obtain the Te@ZIF-8。

Preparation of Te@ZIF-8@Fe(acac)$_3$

In beaker C, a 0.50 g sample of Te@ZIF-8 was completely dissolved in 50 mL of N, N-dimethylformamide (DMF) under ultrasonic treatment to ensure homogeneous dispersion. In beaker D, a 0.50 g sample of Fe(acac)$_3$ was completely dissolved in 50 mL of N, N-dimethylformamide (DMF) under ultrasonic treatment to ensure homogeneous dispersion. The solution from beaker D was transferred into beaker C and stirred at ambient temperature for 24 h. The well-reacted solution was centrifuged, followed by five washing cycles with ethanol, and subsequently dried in an oven at 50 °C for 12 h.

Preparation of Fe-N$_4$/Te-CN

The Te@ZIF-8@Fe(acac)$_3$ was loaded into a porcelain boat and annealed in a tube furnace at 920 °C (heating rate: 2 °C·min^{-1}) under an argon atmosphere for 3 h, yielding a black powder, Fe-N$_4$/Te-CN.

Preparation of ZIF-8

In beaker A, Zn(NO)$_3$·6H$_2$O (5.58 g) was dissolved in 150 mL of the methyl alcohol. In beaker B, 2-methylimidazole was dissolved in 150 mL of the methyl alcohol. After ultrasonically dissolving the solutions in the two beakers respectively, pour the solution in beaker B into beaker A and stir at room temperature for 24 h. The stirred solution was centrifuged, washed five times with ethanol, and dried in an oven at 50 ℃ for 12 h to obtain the ZIF-8。

Preparation of Fe(acac)$_3$@ZIF-8

In beaker C, a 0.50 g sample of ZIF-8 was completely dissolved in 50 mL of N, N-dimethylformamide (DMF) under ultrasonic treatment to ensure homogeneous dispersion. In beaker D, a 0.50 g sample of $Fe(acac)_3$ was completely dissolved in 50 mL of N, N-dimethylformamide (DMF) under ultrasonic treatment to ensure homogeneous dispersion. The solution from beaker D was transferred into beaker C and stirred at ambient temperature for 24 h. The well-reacted solution was centrifuged, followed by five washing cycles with ethanol, and subsequently dried in an oven at 50 °C for 12 h.

Preparation of Fe-N_4/CN

The $Fe(acac)_3$@ZIF-8 was loaded into a porcelain boat and annealed in a tube furnace at 920 °C (heating rate: 2 °C·min^{-1}) under an argon atmosphere for 3 h, yielding a black powder, Fe-N_4/CN.

Characterization

The X-ray photoelectron spectroscopy (XPS) analysis of Fe-N_4/Te-CN, Te-N_4/CN, and Fe-N_4/CN catalysts was conducted using a Thermo Scientific ESCALAB 250 Xi spectrometer equipped with an Al Kα X-ray source. The XPS binding energies for the Fe-N_4/Te-CN, Te-N_4/CN, and Fe-N_4/CN catalysts were referenced to the C 1*s* peak at 284.8 eV for energy calibration. The Raman characterization of Fe-N_4/Te-CN and Fe-N_4/CN was performed via an InVia Micro-Raman spectrometer with 633 nm excitation wavelength. The X-ray diffraction (XRD) patterns of Fe-N_4/Te-CN and Fe-N_4/CN catalysts were collected using a Rigaku RU-200b diffractometer with Cu Kα radiation

(λ = 1.5418 Å). The Fe and Te contents in Fe-N_4/Te-CN and Fe-N_4/CN catalysts were quantified using inductively coupled plasma optical emission spectrometry (ICP-OES). High-resolution HAADF-STEM imaging and corresponding elemental mapping of the Fe-based samples were performed using a JEM-2800 FETEM operated at 200 kV accelerating voltage. The AC-STEM characterization of Fe-N_4/Te-CN and Fe-N_4/CN was performed on a double Cs-corrected JEOL ARM200F TEM (200 keV, 78 pm probe resolution). The surface morphology of the Fe-N_4/Te-CN catalyst was characterized using a JSM-7800F field-emission scanning electron microscope (FESEM) operated at a beam current of 200 nA. The DEMS measurements were conducted under the following conditions: constant potential of –1.0 V *vs.* RHE, total sampling duration of 1800 s with 200 s intervals, 5 measurement cycles, and a catalyst loading of 16 mg.

EXAFS measurement

The Fe K-edge and Te K-edge EXAFS spectra were collected at beamline BL11B of the Shanghai Synchrotron Radiation Facility (SSRF, Shanghai, China) using Si(111) crystal monochromators. For beamline measurements, samples were prepared as thin sheets (1 cm diameter) and hermetically sealed using Kapton tape film. XAFS spectra were acquired at ambient temperature with a Bruker 5040 4-channel silicon drift detector (SDD). EXAFS measurements at the Fe K-edge for Fe-N_4/CN were performed in transmission mode, while fluorescence mode was employed for Fe K-edge and Te K-edge EXAFS characterization of Fe-N_4/Te-CN. The reference samples (Fe foil, FeO, and Fe_2O_3) were characterized by transmission-mode XAFS spectroscopy, with

subsequent data processing and analysis performed using the Athena and Artemis software packages.

EXAFS data analysis

The EXAFS data analysis was performed using Athena software (v0.9.26) for background calibration and pre-edge/post-edge normalization, followed by Fourier transform fitting with Artemis (v0.9.26). For the EXAFS fitting of Fe foil, a k^3-weighted analysis was performed over k-space (3-12 $Å^{-1}$) and R-space (1-3 Å) ranges. The fitting procedures employed k^3 weighting with distinct parameter sets: Fe foil was analyzed with k-range of 3-12 $Å^{-1}$ (R-range: 1-3 Å), while Fe-based samples were fitted using k-range of 3-10.5 $Å^{-1}$ (R-range: 1-2 Å). All four EXAFS fitting parameters-coordination number (CN), bond distance (R), energy shift (ΔE_0), and Debye-Waller factor (σ^2) - were allowed to vary freely during refinement. The k^3-weighted $\chi(k)$ functions were analyzed by wavelet transformation with Cauchy wavelets (n=60) across the k-space range of 2-10 $Å^{-1}$.

Electrocatalytic nitrate reduction

A custom H-configuration glass cell was fabricated to investigate the electrochemical NO_3RR. The cathodic and anodic compartments were isolated by a proton exchange membrane, with the reaction conducted in a neutral medium (0.1 M Na_2SO_4 containing 0.5 M KNO_3) under ambient conditions. The electrochemical performance of NRA was evaluated by measuring the corresponding response using a CHI 760E electrochemical

workstation. A standard three-electrode setup was employed to investigate the electrocatalytic nitrate-to-ammonia conversion. The reference and counter electrodes consisted of an Ag/AgCl electrode (saturated KCl) and a platinum foil, respectively. All measured potentials were referenced against the Ag/AgCl (saturated KCl) electrode and subsequently converted to the reversible hydrogen electrode (RHE) scale using the following equation:

$$E\ (V\ vs.\ RHE) = E\ (V\ vs.\ Ag/AgCl) + 0.0592 \times pH + 0.197$$

The catalyst ink was prepared by homogenizing 8 mg of Fe-based catalyst powder with a mixture of 470 μL ethanol, 470 μL deionized water, and 60 μL Nafion solution via 30-minute ultrasonication. The catalyst ink was uniformly deposited onto a carbon cloth substrate (2 × 2 cm^2), dried under a baking lamp, yielding a catalyst loading of 2 mg cm^{-2}. The electrode maintained an identical geometric area (2 × 2 cm^2) for electrolyte immersion during testing. For NRA, a homogeneous electrolyte containing 0.1 M Na_2SO_4 and 0.5 M KNO_3 was prepared and distributed equally to both electrode chambers. The electrolyte volume was standardized at 30 mL per compartment, with the cathode chamber solution being purged with ultra-high purity argon (99.999%) for 30 minutes preceding electrochemical tests. The cathodic compartment was connected via a gas conduit to a 200 mL sulfuric acid trap (0.0375 M) for continuous absorption of electrochemically generated NH_3 from nitrate reduction. Linear sweep voltammetry (LSV) was performed to evaluate the catalytic activity of Fe-N_4/Te-CN and Fe-N_4/CN for NRA in 0.1 M Na_2SO_4 electrolyte, both with and without 0.5 M KNO_3. To quantify the catalytic differences, the FE (%) and NH_3 generation rates (mg h^{-1} cm^{-2}) of Fe-

N_4/Te-CN and Fe-N_4/CN were measured over a potential window of –1.05 V *vs.* RHE to –1.40 V *vs.* RHE. A constant stirring rate of 650 r.p.m. was maintained in the cathode compartment throughout the measurements. The electrochemical stability of the Fe-N_4/Te-CN catalyst was assessed through chronopotentiometric measurements at a constant current of 120 mA for 3 hours, with the electrolyte maintained at a stirring rate of 650 r.p.m. The cathodic chamber was maintained under continuous high-purity Ar (99.999%) purging during electrochemical testing to ensure complete removal of dissolved O_2 and N_2 species.

The concentrations of NH_3 and nitrite in both electrode compartments and the sulfuric acid trapping solution (0.0375 M) were determined by colorimetric UV-Vis spectrophotometric measurements. All current densities in this study were normalized to the geometric surface area of the working electrode. The NH_3 production rate (mg h^{-1} cm^{-2}) and FE (%) were calculated as follows:

$$\mathrm{NH_3\ yield\ rate} = \frac{\mathrm{m\ (NH_3)\ (mg)}}{t\ \mathrm{(h)} \times S\ (cm^2)}$$

$$\mathrm{FE} = \frac{[\ \mathrm{n\ (NH_3)} \times 8 + \mathrm{n\ (NO_2^-)} \times 2\ ]\ \mathrm{(mol)} \times 96485\ \mathrm{(C\ /\ mol)}}{\mathrm{I\ (A)} \times \mathrm{t\ (s)}}$$

In the preceding equations, m(NH_3) denotes the mass of produced NH_3. In these equations, t denotes the duration of electrolysis, while S corresponds to the geometric surface area of the working electrode. The terms n(NH_3) and n(NO_2^-) correspond to the molar quantities of produced NH_3 and nitrite, respectively.

The TOF was calculated as follows:

$$TOF = N_{NH3\ per\ unite\ area} / N_{active\ site\ per\ unite\ area}$$

$$N_{NH3\ per\ unite\ area} = (Y_{NH3} \times A \times N_A) / 3600$$

$$N_{active\ site\ per\ unite\ area} = (m \times A \times N_A) / M$$

In the preceding equations, $N_{NH3\ per\ unite\ area}$ is the total number of NH_3 turnovers per NH_3 production rates (mol s^{-1}), Y_{NH3} is yield rate of NH_3 (mg h^{-1} cm^{-2}), A is the geometric area of working electrode (4 cm^2), $N_{active\ site\ per\ unite\ area}$ is the number of Fe active sites on the working electrode per unit area (mol), *m* is the Fe atom mass on the working electrode per unit area (g cm^{-2}), measured by the ICP-OES, *M* is the Fe molecular mass used for the calculation of metal active sites.

The DFT calculation

All theoretical calculations in this study were performed using density functional theory (DFT) with the Perdew-Burke-Ernzerhof (PBE) generalized gradient approximation (GGA) for the exchange–correlation functional[S1], as implemented in the Vienna ab initio Simulation Package (VASP)[S2-S3]. Interactions between ion cores and valence electrons were described using the projector augmented wave (PAW) method[S4]. The plane-wave basis was set to 500 eV. For slab models, a vacuum of 15 Å was built, and the Brillouin zone of the reciprocal space was represented by Gamma point, and all calculations were performed with spin-polarization. The convergence criteria are 5×10^{-5} eV for total energy and 0.01 eV/Å for force.

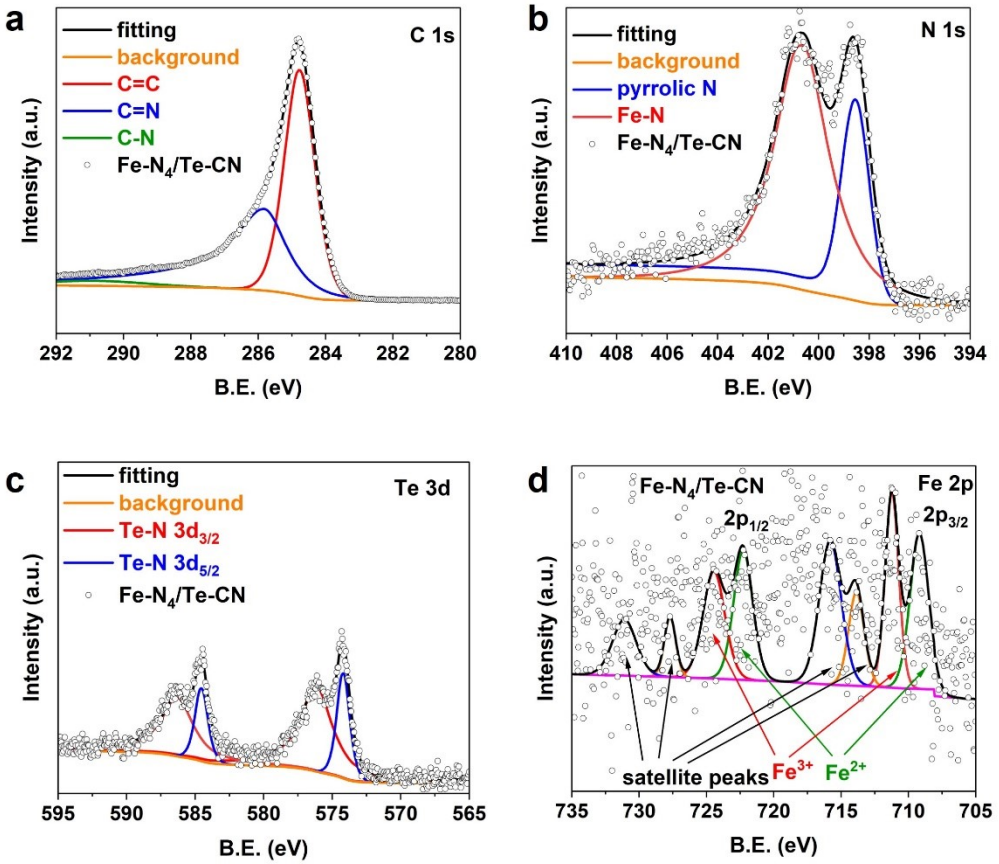

Figure S1. The XPS spectra of Fe-N_4/Te-CN catalyst. a, XPS spectrum for the C 1*s*. b, XPS spectrum for the N 1*s*. c, XPS spectrum for the Te 3*d*. d, XPS spectrum for the Fe 2*p*. The C 1*s* spectrum of Fe-N_4/Te-CN catalyst was composed of the C=C, C=N and C-N bonds (*Appl. Catal. B Environ.*, 2024, **344**, 123643). The N 1*s* spectrum of Fe-N_4/Te-CN catalyst was composed of the pyrrolic N, Fe-N species (*Adv. Funct. Mater.*, 2024, **34**, 2409089). The Te 3*d* spectrum of Fe-N_4/Te-CN catalyst was only composed of the covalent Te from Te-N bond (*Chem Catal.*, 2023, **3**, 100610). The Fe 2*p* spectrum of Fe-N_4/Te-CN catalyst was composed of the Fe^{3+}, Fe^{2+} components and satellite peaks (*Adv. Funct. Mater.*, 2025, **35**, 2504228, *Angew. Chem. Int. Ed.,* 2020, **59**, 13423).

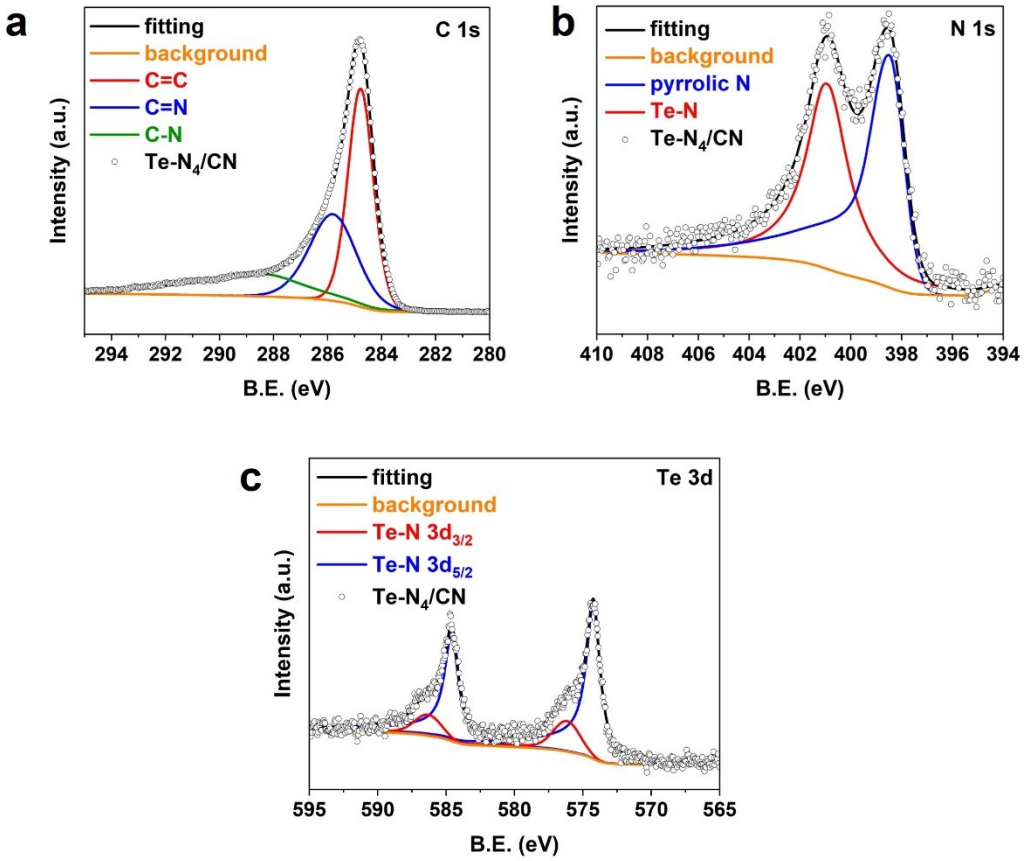

Figure S2. The XPS spectra of Te-N_4/CN catalyst. **a**, XPS spectrum for the C 1*s*. **b**, XPS spectrum for the N 1*s*. **c**, XPS spectrum for the Te 3*d*. The C 1*s* spectrum of Te-N_4/CN catalyst was composed of the C=C, C=N and C-N bonds. The N 1*s* spectrum of Te-N_4/CN catalyst was composed of the Te-N, pyrrolic N species. The Te 3*d* spectrum of Te-N_4/CN catalyst was only composed of the covalent Te from Te-N bond.

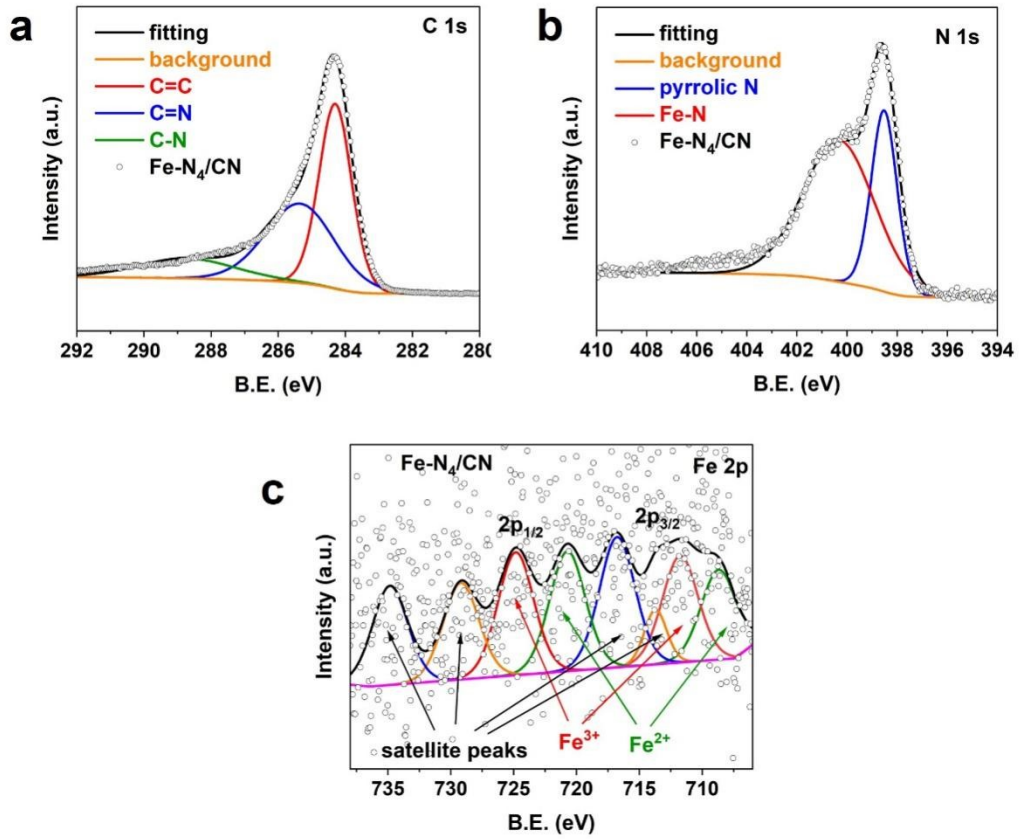

Figure S3. The XPS spectra of Fe-N_4/CN catalyst. a, XPS spectrum for the C 1*s*. b, XPS spectrum for the N 1*s*. c, XPS spectrum for the Fe 2*p*. The C 1*s* spectrum of Fe-N_4/CN catalyst was composed of the C=C, C=N and C-N bonds. The N 1*s* spectrum of Fe-N_4/CN catalyst was composed of the pyrrolic N, Fe-N species. The Fe 2*p* spectrum of Fe-N_4/CN catalyst was composed of the Fe^{3+}, Fe^{2+} components and satellite peaks (*Adv. Funct. Mater*., 2025, **35**, 2504228, *Angew. Chem. Int. Ed.*, 2020, **59**, 13423).

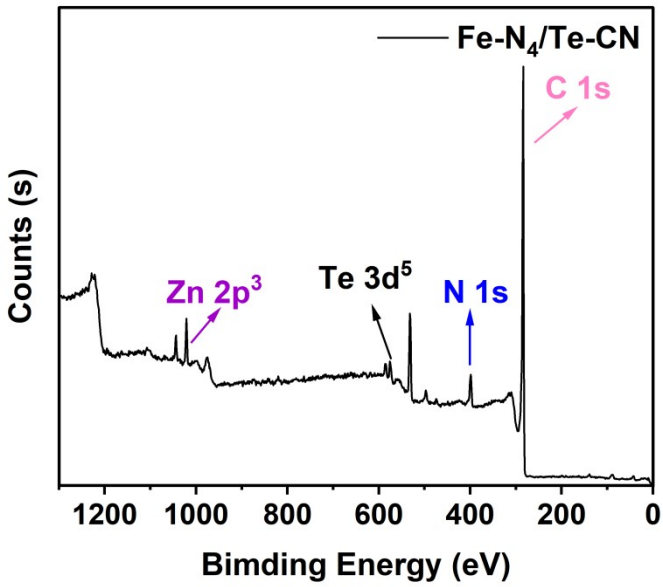

Figure S4. XPS survey spectrum of the Fe-N_4/Te-CN catalyst.

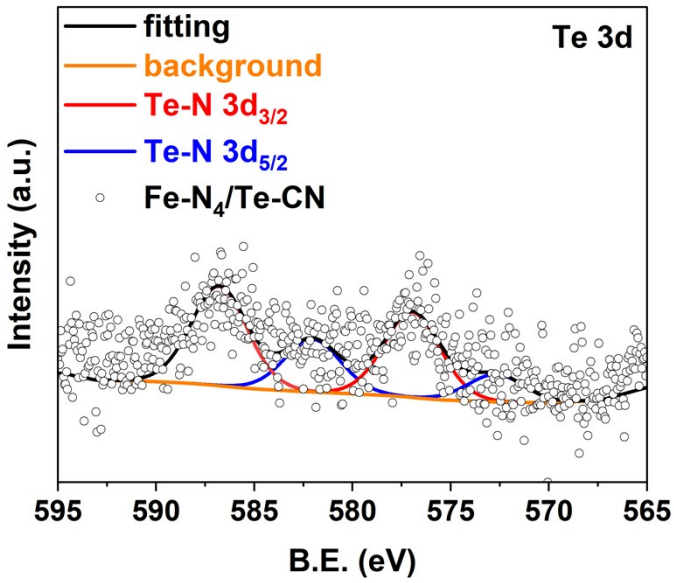

Figure S5. The XPS spectrum for the Te 3*d*.

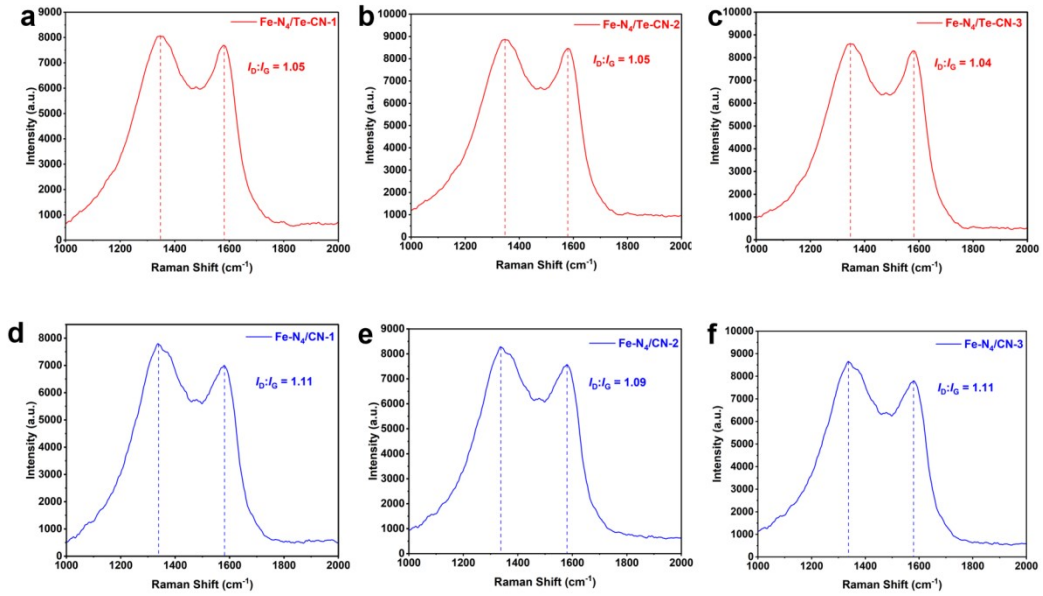

Figure S6. The Raman spectra of (a) the Fe-N_4/Te-CN and (b) the Fe-N_4/CN catalysts, obtained from five independent Raman measurements for each sample, demonstrating the reproducibility of the spectroscopic features.

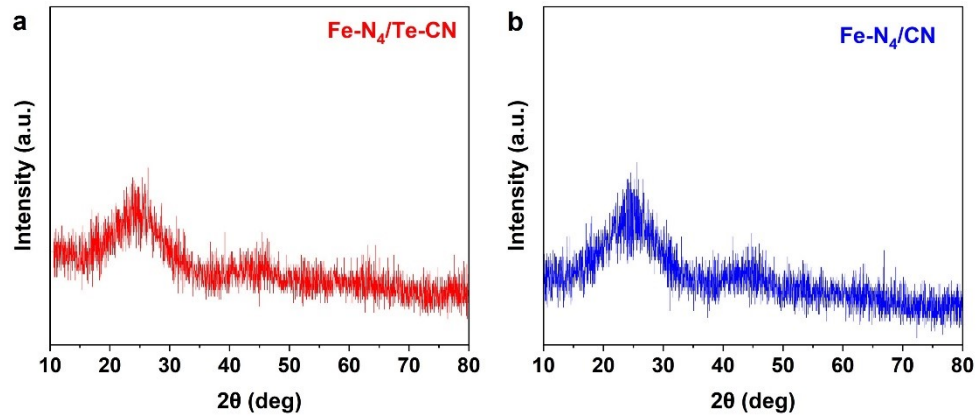

Figure S7. The XRD patterns of (a) the Fe-N_4/Te-CN and (b) Fe-N_4/CN catalysts, respectively.

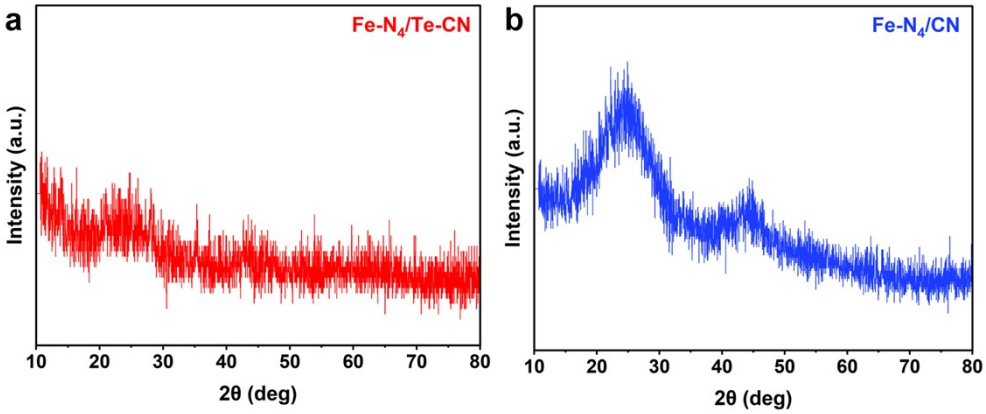

Figure S8. The slow-scan XRD patterns of (a) the Fe-N_4/Te-CN and (b) Fe-N_4/CN catalysts, respectively.

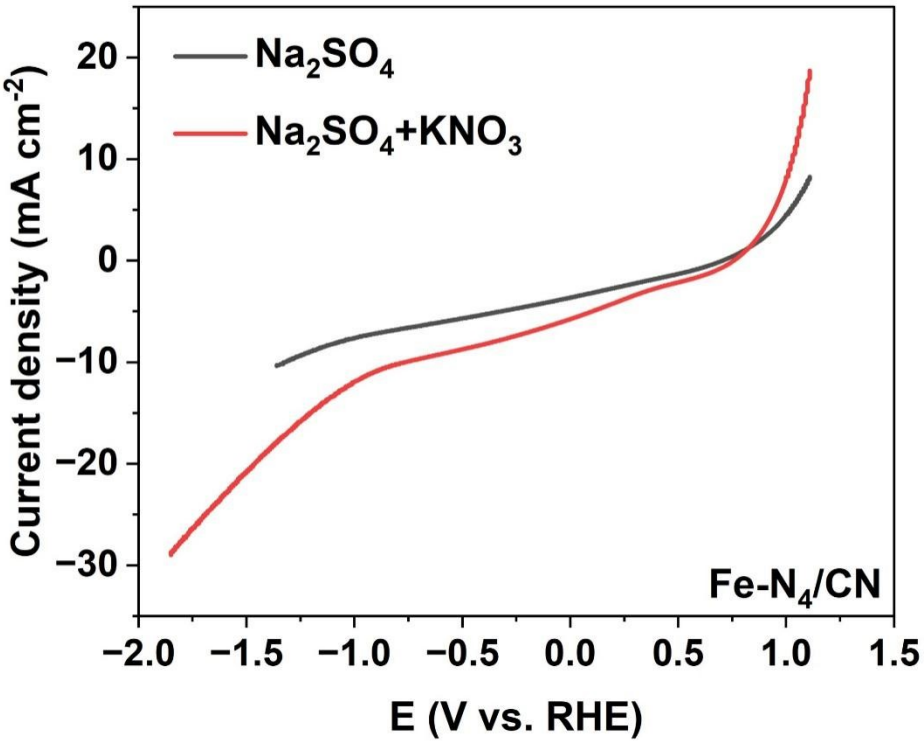

Figure S9. The LSV curves of the Fe-N_4/CN catalyst for NRA in Ar-saturated 0.1 M Na_2SO_4 electrolyte with and without 0.5 M KNO_3.

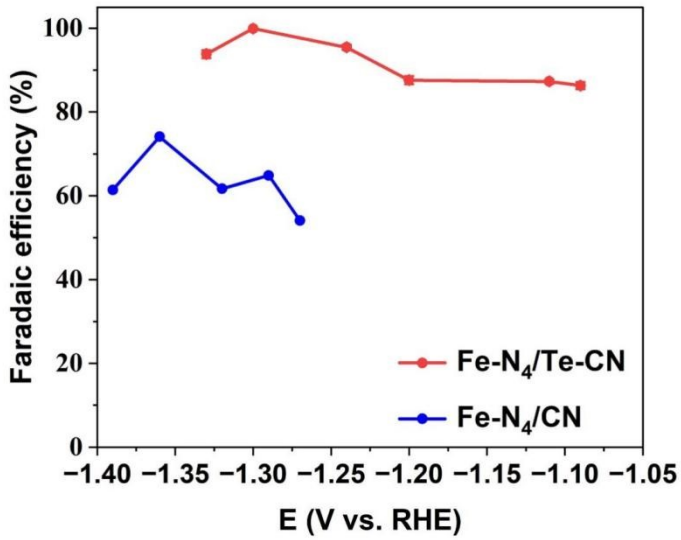

Figure S10. The FE of the Fe-N_4/Te-CN and Fe-N_4/CN catalysts for NRA at different voltages.

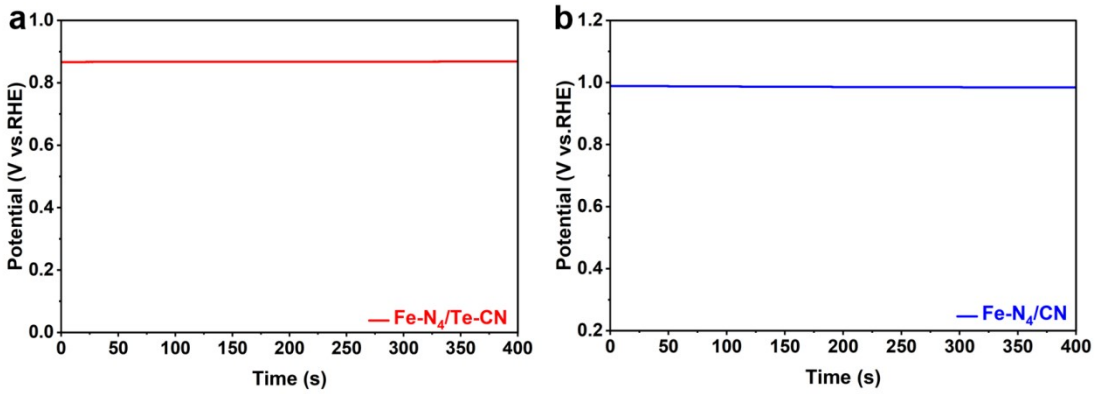

Figure S11. Steady-state open-circuit potentials (OCPs) of the Fe-N_4/Te-CN and Fe-N_4/CN electrodes measured in 0.5 M KNO_3 + 0.1 M Na_2SO_4 electrolyte.

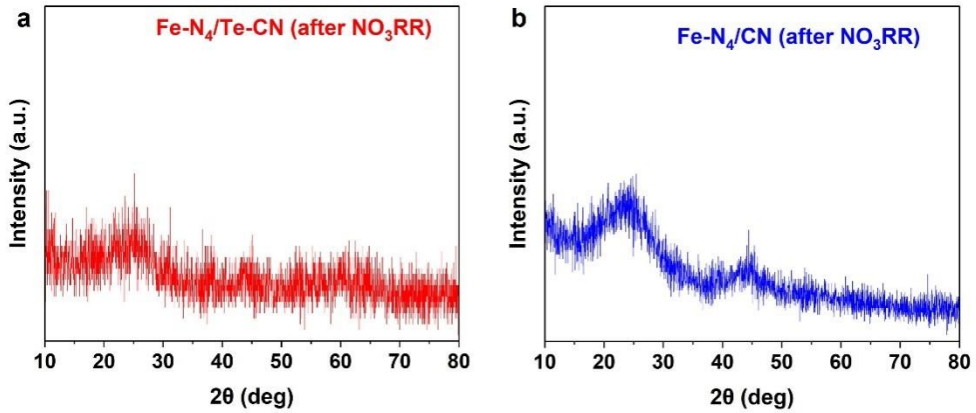

Figure S12. a The XRD of Fe-N_4/Te-CN after NRA. **b** The XRD of Fe-N_4CN after NRA.

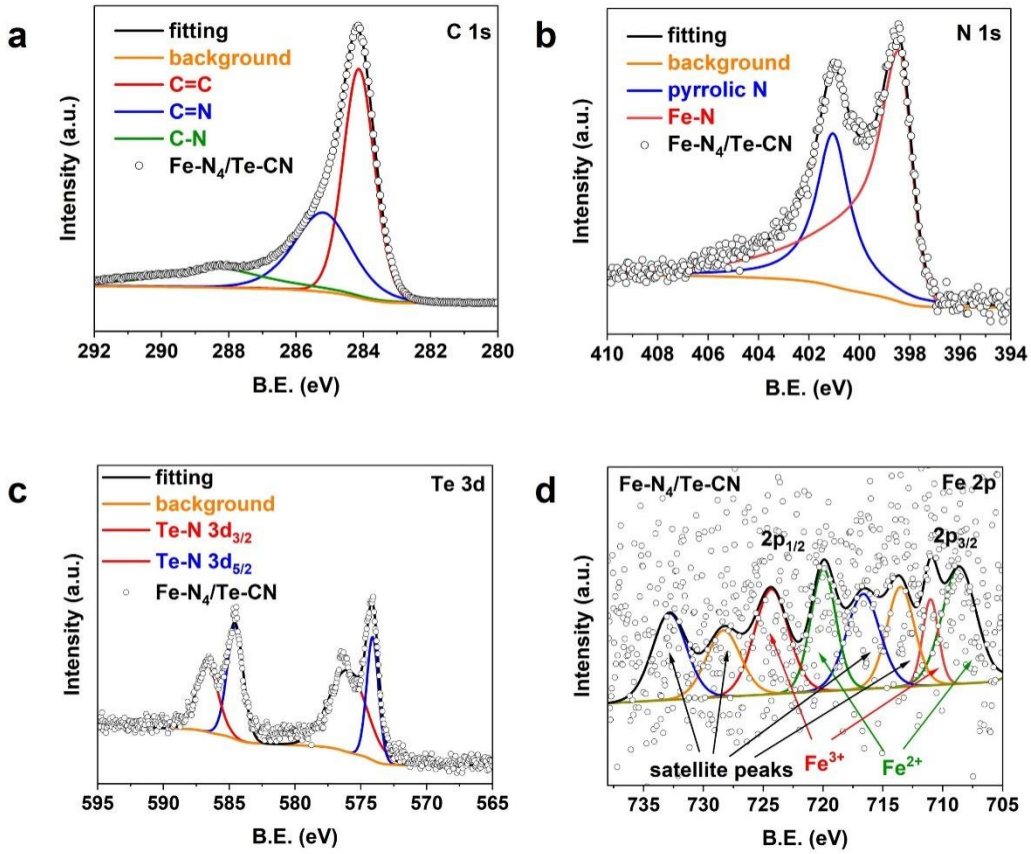

Figure S13. The XPS spectra of Fe-N_4/Te-CN catalyst after NRA. a, XPS spectrum for the C 1*s*. b, XPS spectrum for the N 1*s*. c, XPS spectrum for the Te 3*d*. d, XPS spectrum for the Fe 2*p*.

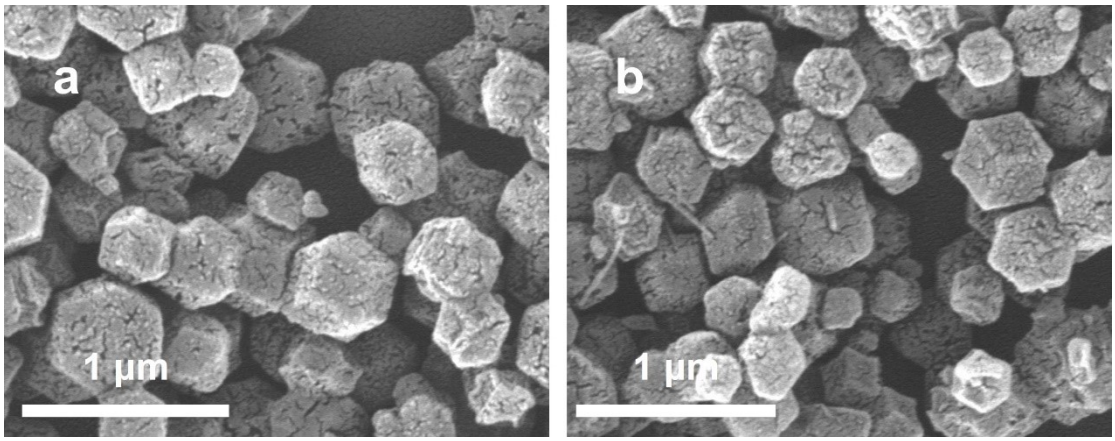

Figure S14. a The FESEM of Fe-N_4/Te-CN before NRA. **b** The FESEM of Fe-N_4/Te-CN after NRA.

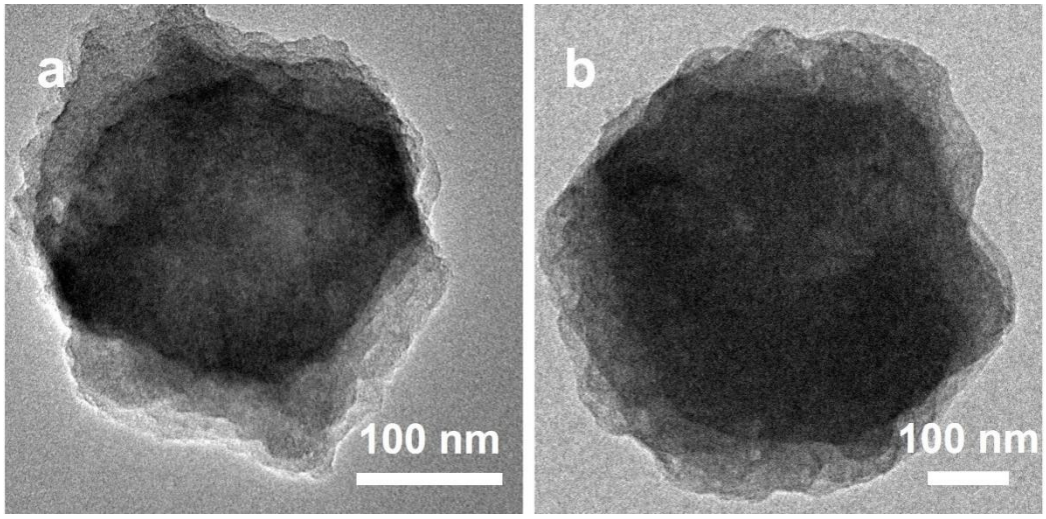

Figure S15. a The TEM of Fe-N_4/Te-CN before NRA. **b** The TEM of Fe-N_4/Te-CN after NRA.

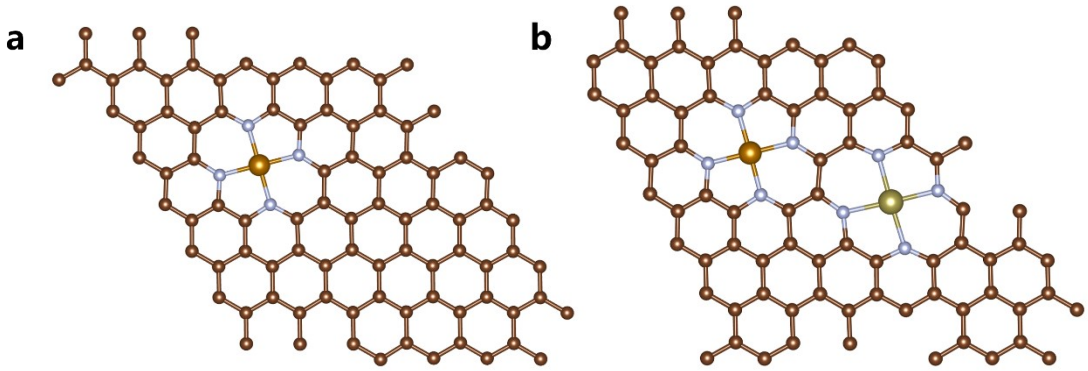

Figure S16. a-b, The model of Fe-N_4 site on N-doped graphene (Fe-N_4/CN model) and the Fe-N_4/Te-CN dual single-atom sites models. The brown, light blue, dark yellow and light yellow balls represented the C, N, Fe and Te atoms, respectively.

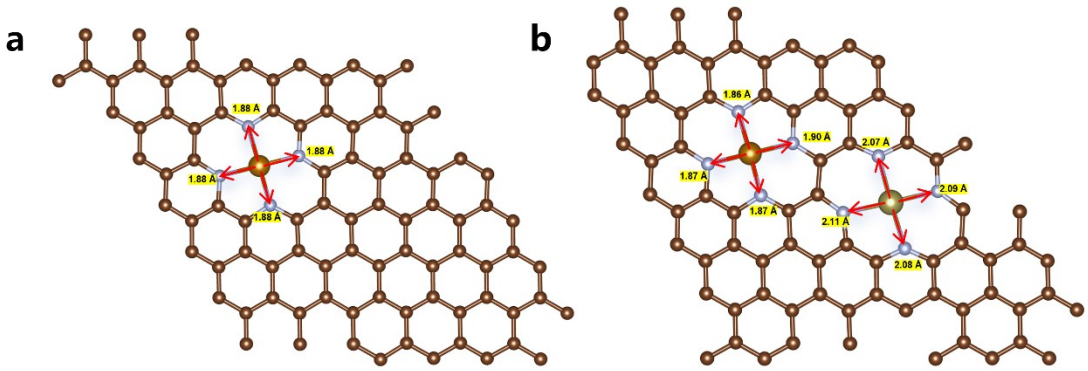

Figure S17. a-b, The symmetric Fe-N bond lengths in Fe-N_4/CN model and the asymmetrical Fe-N and Te-N bond lengths in Fe-N_4/Te-CN model.

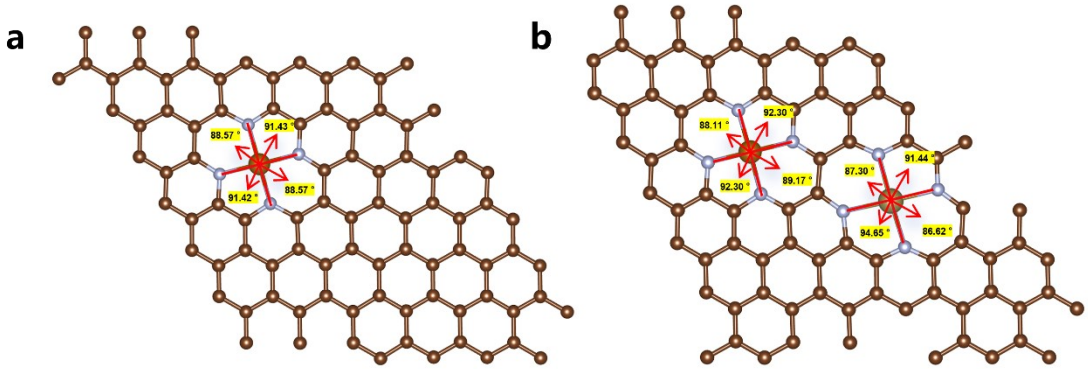

Figure S18. a-b, The symmetric N-Fe-N bond angles in Fe-N_4/CN model and the asymmetrical N-Fe-N and N-Te-N bond angles in Fe-N_4/Te-CN model.

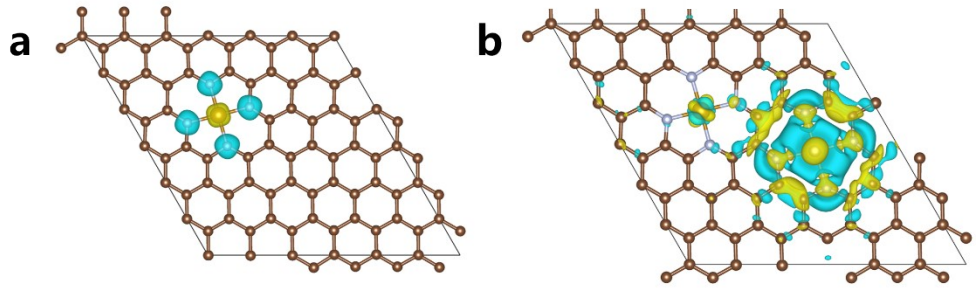

Figure S19. a-b, The symmetric distribution of charge in Fe-N_4/CN model and the asymmetrical distribution of charge in Fe-N_4/Te-CN model.

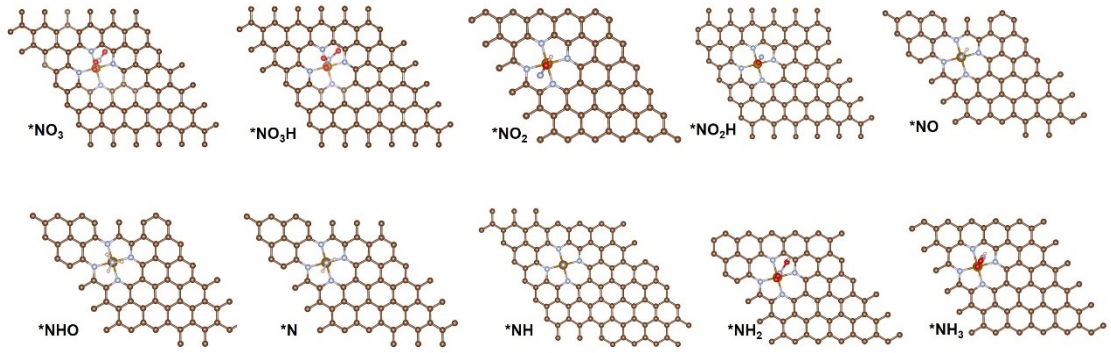

Figure S20. The structures of different N-based intermediates (*NO_3, *NO_3H, *NO_2, *NO_2H, *NO, *NHO, *N, *NH, *NH_2, *NH_3) on the Fe-N_4/CN model for NRA.

Table S1. EXAFS fitting parameters at the Fe K-edge for various samples (S02=0.838).

Sample	Shell	*CN*[a]	*R*(Å)[b]	σ^2 (Å^2·10^{-3}) [c]	ΔE_0(eV)[d]	R factor (%)
Fe-N_4/CN	Fe-N	3.93±0.36	1.92±0.01	0.006	-2.28±1.17	1.02
Fe-N_4/Te-CN	Fe-N	3.76±0.46	1.92±0.01	0.010	-2.71±1.75	1.21

[a]*CN*, coordination number; [b]*R*, distance between absorber and backscatter atoms; [c]σ^2, Debye-Waller factor to account for both thermal and structural disorders; [d]ΔE_0, inner potential correction; *R* factor indicates the goodness of the fit. Fitting range: 3.0 < k (/Å) < 11.0 and 1.0 < R (Å)< 2.5.

Table S2. EXAFS fitting parameters at the Te K-edge for various samples (S02=0.975).

Sample	**Shell**	***CN*[a]**	***R*(Å)[b]**	**σ^2 (Å^2·10^{-3}) [c]**	**ΔE_0(eV)[d]**	**R factor (%)**
Fe-N_4/Te-CN	Te-N	4.11±0.99	1.94±0.02	0.008	-1.01±3.23	1.42

[a]*CN*, coordination number; [b]*R*, distance between absorber and backscatter atoms; [c]σ^2, Debye-Waller factor to account for both thermal and structural disorders; [d]ΔE_0, inner potential correction; *R* factor indicates the goodness of the fit. Fitting range: 3.0 < k (/Å) < 11.0 and 1.0 < R (Å)< 2.5.

Table S3. The comparison of electrocatalytic performances for NRA between Fe-N_4/Te-CN catalyst and other reported catalysts.

Electrocatalyst	Potential (V *vs.* RHE)	NH_3 formation rate	FE (%)	Ref.
Fe-N_4/Te-CN	**–1.30**	**2.19 mg h^{-1} cm^{-2}**	**99.9**	**This work**
Cu_1Fe_3Pc	–1.40	2.4 mmol h^{-1} cm^{-2}	89	S5
Ru-$Co(OH)_2$/CC	–0.48	56501 μg h^{-1} cm_{geo}^{-2}	~96	S6
Ag/NiO	–0.39	0.24 mmol h^{-1} cm^{-2}	94.03	S7
np-Ru/Co_2P	–0.10	23.2 mg h^{-1} cm^{-2}	94.7	S8
MoO_4-CoNi LDH/CuO NW/CF	–0.2	1.12 mmol cm^{-2} h^{-1}	99.78	S9
CuZnFe LDH	–0.9	51 mg h^{-1} cm^{-2}	>95	S10
P-Co/NF	–1.2	223.52 mg h^{-1} cm^{-2}	80	S11
$IrCu_4$	0	12.8 mg h^{-1} cm^{-2}	93.6	S12
Cu_1/hNCNC	–0.58	99.4 mol h^{-1} g_{Cu}^{-1}	99.3	S13
Cu-CoP	–1.0	7.65 mg h^{-1} cm^{-2}	85.1	S14

Table S4. Raw numerical data corresponding to the curves in Figures 3b, including NH_3 yield (mg h^{-1} cm^{-2}) and Faradaic efficiency at each applied potential, provided to facilitate verification of the plotted results.

E (V *vs.* RHE)	Faradaic efficiency (%)	NH_3 yeild rate (mg h^{-1} cm^{-2})
–1.33	93.8	2.16
–1.30	99.9	2.19
–1.24	95.4	1.95
–1.20	87.6	1.68
–1.11	87.3	1.47
–1.09	86.3	1.36

Table S5. Raw numerical data corresponding to the curves in Figures 3c, including NH_3 yield (mg h^{-1} cm^{-2}) and Faradaic efficiency at each applied potential, provided to facilitate verification of the plotted results.

Fe-N_4/CN		Fe-N_4/Te-CN	
E (V *vs.* RHE)	NH_3 yeild rate (mg h^{-1} cm^{-2})	E (V *vs.* RHE)	NH_3 yeild rate (mg h^{-1} cm^{-2})
–1.39	0.84167	–1.33	2.16
–1.36	0.94667	–1.3	2.19
–1.32	0.67367	–1.24	1.95
–1.29	0.60067	–1.2	1.68
–1.27	0.40267	–1.11	1.47
		–1.09	1.36

Table S6. The energies changes for NRA catalyzed on different Fe-based models. (unit: eV)

	Fe-N_4/CN	Fe-N_4/Te-CN
NO_3^-	0	0
*NO_3	0.01	–0.06
*NO_3H	–1.43	–1.36
*NO_2	–1.62	–1.92
*NO_2H	–2.03	–2.01
*NO	–2.56	–2.56
*NHO	–0.58	–0.76
*N	–3.88	–3.72
*NH	–4.68	–4.63
*NH_2	–6.03	–5.98
*NH_3	–7.12	–7.06

Table S7. The dipole moments of Fe-N_4/CN and Fe-N_4/Te-CN models. (unit: e $Å^{-3}$)

models	x	y	z	total
Fe-N_4/CN	–28.3	26.5	0.265	38.8
Fe-N_4/Te-CN	16.9	–106	–2.15	107

References

[S1] J. P. Perde, K. Burke, M. Ernzerhof, *Phys. Rev. Lett.*, 1996, **77**, 3865.

[S2] G. Kresse, J. Furthmüller, *Comput. Mater. Sci.*, 1996, **6**, 15-50.

[S3] G. Kresse, J. Furthmüller, *Phys. Rev. B: Condens. Matter Mater. Phys*., 1996, **54**, 11169-11186.

[S4] P. E. Blöchl, *Phys. Rev. B,* 1994, **50**, 17953.

[S5] J. Y. Feng, Q. K. Hu, X. Yue, Q. Chen, C. Q. Gao, J. Gu, L. Zhang, L. Y. Zhang, H. Dai, F. Yang, G. C. Lin, K. P. Loh. Z. X. Xu, *Appl. Catal. B-Environ*. 2025, **366**, 125027.

[S6] L. C. Zhang, J. Z. Y. Seow, Y. Liu, L. Li, T. Wu, Q. Wu, X. Lin, S. Sun, L. Tannesia, K. Tang, D. S. Shao, S. B. Xi, X. D. Guo, Z. C. J. Xu, *Energy Environ. Sci.* 2025, **18**, 5622.

[S7] R. X. Zhong, S. M. Lv, H. Wang, Y. M. Jiang, R. X. He, M. Li, *Mater. Today Chem.*, 2025, **44**, 102570.

[S8] Y. D. Huang, Y. Q. Liang, H. Jiang, S. L. Wu, Z. Y. Li, Z. H. Gao, Z. D. Cui, S. L Zhu, W. C. Xu, *Chem. Eng. J.*, 2025*,* **516**, 164046.

[S9] C. Z. Lin, W. J. Li, H. Chen, J. T. Feng, M. Y. Zhu, J. W. Shi, M. T. Li, B. Hou, Z. Y. Wang, X. Chen, J. Liu, W. Yan, *Adv. Sci.*, 2025, **12**, 2502262.

[S10] J. Q. Kang, Y. X. Xiao, L. Li, L. L. Qiao, C. F. Liu, C. C. Zhong, P. Z. Sun, D. Liu, W. F. Ip, and H. Pan, *Adv. Funct. Mater.,* 2025, **35**, 2507619.

[S11] L. B. Zuo, F. C. Lou, J. T. Guo, M. Wang, S. Geng, *Chem. Eng. J.*, 2025*,* **517**, 163630.

[S12] N. He, Z. Yuan, C. Wu, S. B. Xi, J. J. Xiong, Y. C. Huang, G. W. Lian, Z. F. Du, L. H. Liu, D. W. Wu, Z. X. Chen, W. G. Tu, Z. G. Zou, S. Y. Tong, *ACS Nano*, 2025, **19**, 4684.

[S13] Z. Shen, F. F. Xu, X. Y. Cheng, J. T. Jiang, C. K. Zhou, Y. Zeng, X. Z. Wang, L. J. Yang, Q. Wu, Z. Hu, *ACS Nano*, 2025**, 19**, 4611.

[S14] W. H. Yang, Z. W. Chang, X. Yu, P. Wu, R. X. Shen, L. Z. Wang, X. Z. Cui, J. L. Shi, *Adv. Sci.*, 2025, **12**, 2416386.